Article

Design of a Freeform Surface Optical Detection System with a Square Aperture

Hongkai Zhao [1,2,3] and Xianglong Mao [1,2,3,*]

1 Key Laboratory of Spectral Imaging Technology of CAS, Xi'an Institute of Optics and Precision Mechanics, Chinese Academy of Sciences, Xi'an 710119, China; zhaohongkai2022@opt.ac.cn
2 University of Chinese Academy of Sciences, Beijing 100049, China
3 Shanxi Key Laboratory of Optical Remote Sensing and Intelligent Information Processing, Xi'an 710119, China
* Correspondence: maoxianglong@opt.ac.cn

Abstract: To meet the demands for heightened detection sensitivity in satellite-based space target detection systems, we introduce an innovative square aperture diaphragm system utilizing freeform surfaces for detecting targets in the visible light spectrum. Characterized by a 40 mm × 40 mm square entrance pupil, a 4° × 4° field of view (FOV), and a 150 mm focal length, this system achieves a spot size of 2 × 2 pixels with 85% energy concentration within 18.4 μm, showcasing exceptional performance. Our design, compared to a circular aperture system of similar specifications, increases the entrance pupil area by 27% while having a smaller volume, resulting in a 0.24 magnitude improvement in the detection of space targets. This advancement significantly enhances our ability to detect fainter space targets with high sensitivity. The findings of this study pave the way for advancements in satellite-based space target detection technology.

Keywords: freeform optics; satellite-based detection system; space target; detection sensitivity; square aperture diaphragm; entrance pupil area

1. Introduction

As global space exploration advances, the number of spacecraft in orbit continues to grow, along with the rising number of non-operational satellites and collision-derived debris [1]. Collectively, these are known as space targets. To address the challenges that the growing number of space targets presents to the secure operation of orbiting spacecraft, all space-faring countries are actively engaged in the development of space target detection systems [2,3].

Satellite-based space target detection systems on board various types of space satellites have incomparable advantages over ground-based space target detection systems, because they operate in the space environment and are not affected by atmospheric interference and bad weather [1]. The off-axis three-mirror optical system is widely used in the field of satellite-based space target detection because of no center blocking, no chromatic aberration, and long focal length. The SBV camera mounted on the United States SBX satellite operates at F/3 with a concentration of energy in the image plane greater than 60 percent and a 1.5° × 6.6° FOV [4]. The optical system mounted on the WASSS has a 60° × 4° FOV, enabling continuous surveillance of space targets in a relatively short period of time [5].

Off-axis reflective systems are difficult to design to achieve the desired specifications based on existing designs due to the lack of an initial structure for the design. As such, many methods for solving the initial structure of free-form optical systems have appeared. For example, the Nodal Aberration theory. Bauer et al. designed and obtained a freeform

off-axis three-mirror optical system with a 200 mm entrance pupil diameter, an F-number of 3, and a 4° × 4° FOV [6]. Another example is the partial differential equation (PDE) method. Hicks realized large FOV optical system using the partial differential equation method [7]. Another is the simultaneous multiple surface (SMS) method where Miñano et al. designed a coaxial optical system with four curved surfaces using the SMS design method to achieve precise control of four beams [8]. The construction–iteration (C-I) method, where Yang et al. designed a system that operates at F/1.49 with a 64 mm entrance pupil diameter and an 8° × 9° FOV [9].

Freeform surfaces generally refer to surfaces without rotational symmetry. Freeform surfaces are characterized by XY polynomials, Zernike polynomials, Q-polynomials, Legendre polynomials, and Chebyshev polynomials, among others. Compared with traditional spherical and aspherical surfaces, freeform surfaces have higher degrees of freedom and stronger ability of aberration correction, and have been increasingly used in the design of imaging and non-imaging optical systems [10–20].

In the field of satellite-based space target detection, detection sensitivity is an important index to determine the detection capability of the system, which determines whether the satellite-based space target detection system can detect the light reflected from the target or the background star. In order to improve the detection sensitivity of the satellite-based space target detection system, it is necessary to increase the entrance pupil area of the optical system while keeping the volume unchanged.

To enhance the detection sensitivity of existing satellite-based space target detection systems with circular aperture diaphragms, there is a requirement to enlarge the entrance pupil diameter. However, this enlargement will inevitably result in an increase in system volume, which is not desirable for satellite-based systems due to their constraints on size and weight. Meanwhile, non-circular aperture diaphragms have been applied in imaging systems [21] and imaging spectrometer systems [22], among others. However, they have yet to find applications in the field of detection, highlighting a significant gap in the field's system design.

To fulfill the demand for improved detection sensitivity in satellite-based space target detection systems, this paper introduces a novel design of a square aperture freeform surface space target detection system. The final system operates at F/3.3 with a 40 mm × 40 mm square entrance pupil, a 2 × 2 pixel image spot, an 85% energy concentration within 18.4 μm and a 4° × 4° FOV. Compared with the circular aperture diaphragm system with the same volume limit, it is verified that the square aperture diaphragm system achieves a larger entrance pupil area. Therefore, the square aperture diaphragm system enhances the detection capability for space targets, enabling it to detect fainter space targets.

2. Materials and Methods

2.1. Theoretical Basis

2.1.1. Space Target Detection Sensitivity Model

Satellite-based space target detection involves a sophisticated photoelectric conversion process. As depicted in Figure 1, the sunlight and starry background light reflected by space targets traverse space, penetrate the optical system, are captured on the focal plane detector, and ultimately transformed into an image via signal processing circuitry.
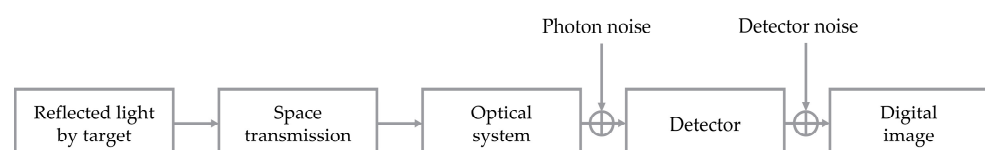
Figure 1. The process of transmitting and imaging the reflected light from space targets.

In the realm of satellite-based detection, the faintest magnitude that a system can detect is often considered the paramount indicator of the camera's detection capability. Magnitude serves as a measure of the brightness of stars or other celestial objects, with a 100-fold difference in irradiance corresponding to a difference of five magnitudes. The smaller the irradiance, the greater the magnitude. Based on the optical radiation theory, noise model, and the signal-to-noise ratio (SNR), Equation (1) establishes the detection sensitivity model for space targets [23]. This model dictates that a space target can be detected only if the reflected light at the optical system's pupil achieves the magnitude specified by Equation (1):

$$\text{m} \leq -\log_{2.512}\left[\frac{683 \times 10^6}{21.2} \times \frac{\left[\text{T}_{\text{sn}}^2 + \sqrt{\text{T}_{\text{sn}}^2 + 4(\text{N}_\text{D} + \text{N}_\text{B})\text{T}_{\text{sn}}^2}\right]\pi\text{d}^2\text{hc}}{\overline{\lambda}\text{S}_\text{d}\eta\tau_0\text{a}^2}\right] \quad (1)$$

where m is the magnitude of a space target as observed at the entrance pupil of the optical system, $\overline{\lambda}$ is the average wavelength, S_d is the effective pupil area of the optical system, η is the average quantum efficiency, τ_0 is the transmittance of the optical system, N_B is the number of photoelectrons generated by background noise, N_D is the number of photoelectrons generated by dark current, T_{sn} is the SNR threshold required to meet a certain detection rate and false alarm rate, a is the size of the detector's single pixel size, d is the diameter of the image spot, h is the Planck's constant, and c is the speed of light.

In light of qualitative analysis in Equation (1), the ensuing conclusion can be derived: given that the system volume remains invariant, amplifying the entrance pupil area of the system will augment the detection sensitivity of the system.

2.1.2. Description of Freeform Surfaces

In the design of an optical system with freeform surfaces, it is essential to meet the predefined specifications and impose extra constraints to mitigate the fabrication challenges inherent in freeform surfaces. The precision of freeform surface measurements is a key determinant of the manufacturing precision of these surfaces. Zero-position interferometry stands out as a prevalent high-precision technique for assessing freeform surfaces. This method involves the design and production of computational holographic elements (CGH), which are engineered to alter the base surface wavefront to align with the surface under test. To simplify the fabrication of CGH and, by extension, the complexity of surface measurement, it is essential to minimize the sag departures between the freeform surface and the base surface [22,24].

For non-orthogonal XY polynomial freeform surfaces, the sag departures relative to the base surface must be calculated and managed by sampling discrete points across the surface. However, when the sampling density is high, system optimization becomes sluggish and inefficient due to the sheer number of variables involved. Employing orthogonal polynomial freeform surfaces offers a straightforward solution to the sluggish optimization dilemma. This is because the sum of the squares of the coefficients of these orthogonal polynomials bears a direct mathematical relationship to the sag departures between the freeform surface and the base surface, simplifying the optimization process.

For rectangular apertures, both Chebyshev and Legendre polynomials, which exhibit orthogonality within the square domain, are adept at significantly and efficiently minimizing the sag deviations between the freeform surface and the base surface. This reduction in deviation simplifies the challenges associated with surface measurement and manufacturing [22]. In this study, preference is given to Chebyshev polynomials for optical system design, leveraging their direct applicability within the Zemax optical design software.

The one-dimensional Chebyshev polynomials in the *x*-axis are orthogonal with respect to their associated weight function across the interval [−1, 1], as illustrated in Equation (2). A similar orthogonality applies to the *y*-axis:

$$\int_{-1}^{1} \frac{T_m(x)T_n(x)}{\sqrt{1-x^2}} dx = \begin{cases} 0.5\pi\delta_{mn}, & \text{when } m \neq 0, n \neq 0 \\ \pi, & \text{when } m = n = 0 \end{cases} \tag{2}$$

where δ_{mn} is the Kronecker function, when $m = n$, $\delta_{mn} = 1$; when $m \neq n$, $\delta_{mn} = 0$. Table 1 shows the first six terms of the non-normalized Chebyshev polynomial in the x-direction.

Table 1. One-dimensional Chebyshev polynomial up to the sixth order.

n	$T_n(u)$
0	1
1	u
2	$2u^2 - 1$
3	$4u^3 - 3u$
4	$8u^4 - 8u^2 + 1$
5	$16u^5 - 20u^3 + 5u$
6	$32u^6 - 48u^4 + 18u^2 - 1$

Two-dimensional polynomials are derived by multiplying the one-dimensional polynomials along the x and y axes. The polynomial surfaces are then constructed by superimposing the base surface with these two-dimensional polynomials. The resulting expression is:

$$z(x,y) = \frac{c(x^2 + y^2)}{1 + \sqrt{1 - (1+k)c^2(x^2 + y^2)}} + \sum_{i=0}^{M} \sum_{j=0}^{N} \alpha_{i,j} \cdot T_i(u)T_j(v) \tag{3}$$

where c is the curvature at the vertex of the base surface; k is the quadratic surface coefficient; $T_i(u)$ and $T_j(v)$ is the one-dimensional Chebyshev polynomial; $u = x/x_0$, $v = y/y_0$, x_0, and y_0 are the normalized aperture values in the x and y directions, such that the rectangular region is normalized to a unit-square domain of side length 2; M and N are the orders of the Chebyshev polynomials in the x and y directions; and $\alpha_{i,j}$ are the corresponding polynomial coefficients. The Chebyshev polynomials used subsequently in this paper are symmetric about the YOZ plane and do not contain odd-numbered terms of x.

Given that the weight function of the Chebyshev polynomial is tied to the independent variables, it is not feasible to directly limit the sum of the squares of the coefficients when managing the sag departures of the freeform surfaces of the Chebyshev polynomials during the optimization process. Nonetheless, it is achievable to mitigate the sag departures within the rectangular aperture by regulating the sum of the sag departures at the edges of the aperture to achieve a zero mean [22]. This approach simplifies the complexity of surface measurement.

Taking into account the even terms in the Chebyshev polynomial of degree 6, the summation of the sag departures at the edges of the rectangular domain results in [22]:

$$zsag_{sum} = 8\alpha_{0,0} + \frac{8}{3}(\alpha_{0,2} + \alpha_{2,0} - \alpha_{2,2}) + \frac{56}{15}(\alpha_{0,4} + \alpha_{4,0}) + \frac{136}{15}(\alpha_{0,6} + \alpha_{6,0}) - \frac{8}{5}(\alpha_{2,4} + \alpha_{4,2}) \tag{4}$$

where the parameter $zsag_{sum}$ is associated with the outcome of linear operations on certain polynomial coefficients. This relationship can be leveraged during the design phase by imposing constraints to set these coefficients to zero, thereby managing the complexity of surface measurement. To counteract the piston and tilt terms inherently introduced by the

polynomial, additional constraints are imposed to ensure that the linear combination of specific coefficients equals zero [22], as follows:

$$\text{piston} = \alpha_{0,0} - \alpha_{2,0} - \alpha_{0,2} + \alpha_{4,0} + \alpha_{2,2} + \alpha_{0,4} - \alpha_{6,0} - \alpha_{4,2} - \alpha_{2,4} - \alpha_{0,6} = 0 \tag{5}$$

$$\text{tilt} = \alpha_{0,1} - 3\alpha_{0,3} + 5\alpha_{0,5} - \alpha_{2,1} + 3\alpha_{2,3} + \alpha_{4,1} = 0 \tag{6}$$

2.2. Design of Square Diaphragm System

2.2.1. Specification of Square Aperture Diaphragm System

Table 2 presents the design specifications for an off-axis three-mirror optical system featuring a square diaphragm.

Table 2. Design specifications of optical system with square aperture diaphragm.

Parameter	Specifications
Spectral band	0.4 μm~0.9 μm
FOV	$4° \times 4°$
Focal length	150 mm
Entrance pupil	40 mm × 40 mm
Equivalent F-number	3.3
Volume	$\leq 1 \text{ dm}^3$
Detector pixel size	9.2 μm × 9.2 μm
Image spot size	$\leq$18.4 μm × 18.4 μm
Distortion	$\leq 1\%$

2.2.2. Preliminary Optimization of Square Aperture Diaphragm System

Drawing from the design specifications detailed in Table 2, we selected and optimized a three-mirror system to construct an unobstructed off-axis optical configuration, situating the aperture diaphragm on the primary mirror. Through localized optimization in Zemax and the incorporation of a merit function, we effectively managed mirror collisions and prevented light obstruction. We also controlled the focusing of the central light onto the mirror's center, the convergence of light onto the image plane, the curvature radius of the mirrors, the spacing and size of the mirrors, and the tilting of mirrors along with distortion. After preliminary optimization, the average RMS spot size was approximately 400 μm. Figure 2 shows the three-dimensional (3D) view of the preliminary optical system and the spot diagrams for each FOV. Table 3 provides a detailed breakdown of the preliminary system's mirror specifications, including the curvature radius of mirrors M1 to M3, the spacing between the mirrors, and their respective deflection angles.
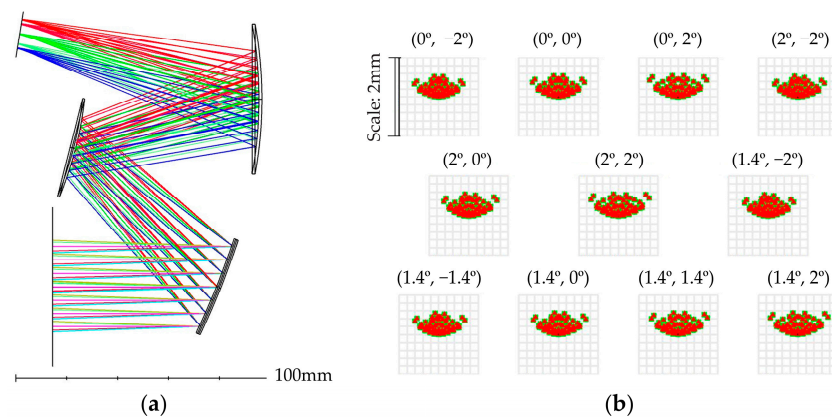
Figure 2. (**a**) The layout and (**b**) the spot diagrams of the preliminary system.

Table 3. Structural parameters of the preliminary optical system.

Surface	Surface Type	Radius/mm	Thickness/mm	X Tilt/°
Object Surface	Standard	Infinity	Infinity	
1	Standard	Infinity	65	
2	Coordinate Break		0	22.00
PM (Stop)	Standard	−333.96	0	
4	Coordinate Break		−77.85	22.00
5	Coordinate Break		0	−29.53
SM	Standard	−143.83	0	
7	Coordinate Break		74.68	−29.53
8	Coordinate Break		0	15.09
TM	Standard	−162.89	0	
10	Coordinate Break		−97.42	15.09
11	Coordinate Break		0	−5.85
Image Surface	Standard	Infinity		

2.2.3. Further Optimization Based on the C-I Algorithm of Square Aperture Diaphragm System

Lacking a pre-existing initial structure for a detection system with a square aperture freeform surface, we employed algorithms to determine an optimal initial structure for the optical system, which is crucial. The construction–iteration (C-I) algorithm, which begins with a three-sphere design approach, was selected for this purpose. In the initial surface construction process, the coordinates as well as the surface normals of the data points on the multiple freeform surfaces were calculated directly considering the rays of multiple field angles and different square pupil coordinates. Then, an iterative process was employed to improve the image quality [25].

In the initial construction process, the FOV and aperture were first sampled. We selected 11 specific fields of view: $(0°, −2°)$, $(0°, 0°)$, $(0°, 2°)$, $(2°, −2°)$, $(2°, 0°)$, $(2°, 2°)$, $(1.4°, −2°)$, $(1.4°, −1.4°)$, $(1.4°, 0°)$, $(1.4°, 1.4°)$, and $(1.4°, 2°)$. The rectangular aperture was evenly divided into 31 segments in both the x and y directions, resulting in a total of 10,571 characteristic rays. Using Matlab, we established a connection to Zemax via its interactive extension to perform ray tracing, obtaining the starting coordinates and direction vectors for these characteristic rays. Subsequently, we developed an algorithm in Matlab, based on the object–image relationship and the shortest ray algorithm [9], to calculate the feature coordinate points on the surface one by one, along with the corresponding normal vectors at these feature points. The expression for the freeform surface was then derived by applying a fitting method [26] that took into account both the three-dimensional (3D) coordinates and normal vectors of the discrete data points. The construction process was finalized by sequentially constructing all surfaces in this manner.

Following the initial construction, an iterative process was initiated. The same 11 fields of view were selected, and the rectangular aperture was divided into 51 equal parts in both the x and y directions, yielding a total of 28,611 feature rays. Ray tracing was used to determine the intersection points of these feature rays with the surfaces designated for iteration. Subsequently, an algorithm was developed based on Fermat's principle [27] and the object–image relationship to calculate the corresponding normal vectors at the feature points, allowing us to ascertain the normal vectors for all feature points. The freeform surface expressions for the iterative surfaces were then derived using a fitting method that took into account both the 3D coordinates and the normal vectors. This iterative process was carried out for each surface individually. Finally, the surface expressions obtained through this algorithm were fitted using XY polynomials to represent the surfaces.

After the C-I algorithm and simple routine optimization in Zemax, a better initial structure was obtained, as shown in Figure 3. Using this algorithm and the following optimization in Zemax, compared to direct optimization starting with a tri-spherical off-axis three-mirror system, results in a system with smaller spot sizes, greater energy concentration, and reduced wavefront aberration. Due to space constraints, the detailed comparison is not presented here. For systems demanding high specifications and precision, employing the C-I algorithm to obtain a superior initial structure is crucial before proceeding with system optimization. Figure 3 illustrates the 3D view and spot diagrams of the optical system after applying the C-I algorithm and simple routine optimization. This optimized optical system serves as the foundation for further design work.
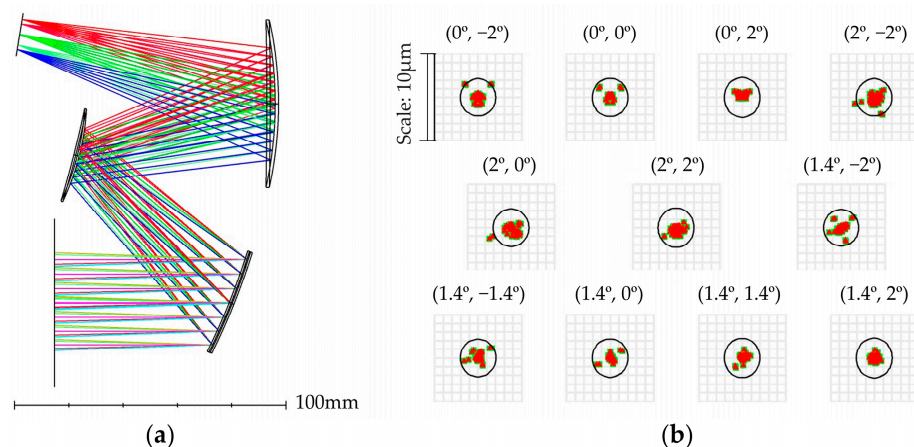
Figure 3. (**a**) The layout and (**b**) the spot diagrams through the C-I algorithm and the following optimization in Zemax.

2.2.4. Final Optimization of Adding Manufacturing Constraints to a Square Aperture Diaphragm System

We utilized the optical system depicted in Figure 3 as the foundation for further optimization. The 3D coordinate points and normal vectors on M1~M3 were obtained by ray tracing using Matlab and Zemax interactive extensions and refitted to Chebyshev polynomials. In particular, it is noted here that such a complex fitting process was used because the design results obtained from Section 2.2.3 using the C-I algorithm with discrete points and normal vectors first fitted to XY polynomials and then interactively fitted to Chebyshev polynomials were superior to the results of a direct fit to Chebyshev polynomials.

Mirrors M1 to M3 were defined by 6th order even Chebyshev polynomials, symmetric around the YOZ plane. Subsequently, the three manufacturing constraints from Equations (4)–(6) were incorporated into the optimization process, along with the default optimization operands. These default operands were initially based on the image spot size, and then on contrast, generated by the system. The optimizations—first for spot size and then for contrast—form one cycle. Multiple cycles were conducted, and the system optimization ended after the ninth cycle when the system's performance met the specified requirements.

Figure 4 depicts the final optimization design workflow for the three-mirror off-axis system with a square aperture diaphragm.
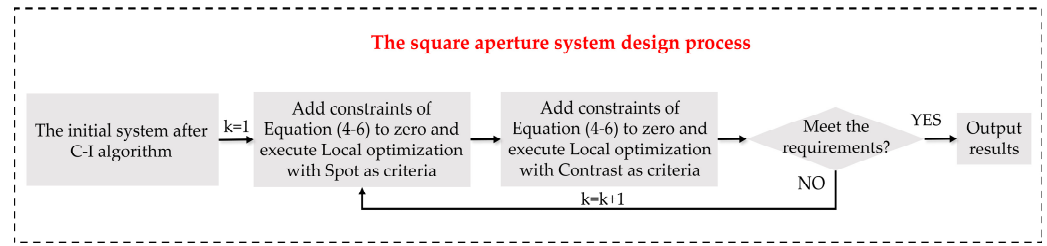
Figure 4. The design flow of the final optimization process of adding constraints to the square aperture diaphragm system.

It was observed that the peak to valley (PV) value of the sag departures between the surface and the base surface decreased in tandem with the reduction in the sum of the sag departures at the edges of the rectangular region, as depicted in Figure 5. Specifically, the PV value of the sag departures for the primary mirror decreased from 1.38 mm to 0.06 mm, for the secondary mirror from 1.62 mm to 0.28 mm, and for the tertiary mirror from 4.52 mm to 0.24 mm. This demonstrates that by controlling the sum of the sag departures between the surface and the base surface at the edge of the rectangular region to zero, the PV value of the sag departures is effectively reduced, which significantly simplifies the process of surface measurement.
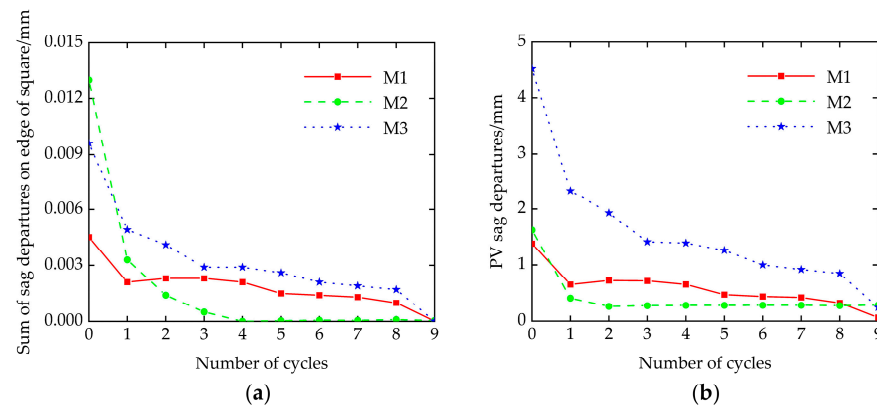
Figure 5. (**a**) The sum of sag departures on edge of square and (**b**) the PV value of the sag departures of each mirror in square aperture system during optimization with manufacturing constraints.

The final off-axis three-mirror optical system, defined by 6th order even Chebyshev polynomials and featuring a square aperture, was successfully engineered in accordance with the preset metrics after incorporating manufacturing constraints and undergoing nine optimization cycles with spot size and contrast as the key optimization metrics. The primary mirror incorporated a square aperture diaphragm measuring 40 mm by 40 mm, while the base spherical surfaces of mirrors M1, M2, and M3 had radius of curvature at -341.964 mm, -112.864 mm, and -159.690 mm, respectively. The system was designed with a focal length of 150 mm and an FOV spanning 4° by 4°. The volume of the square aperture diaphragm system was $50 \times 140 \times 112$ mm^3, that is, 0.78 cubic decimeters, less than the preset requirement of 1 cubic decimeter. Figure 6 presents the 3D view of the system along with the ray footprints on mirrors M1 to M3 and the image plane. Table 4 shows the coefficients of the Chebyshev polynomials for mirrors M1 to M3 of the final system with square aperture.
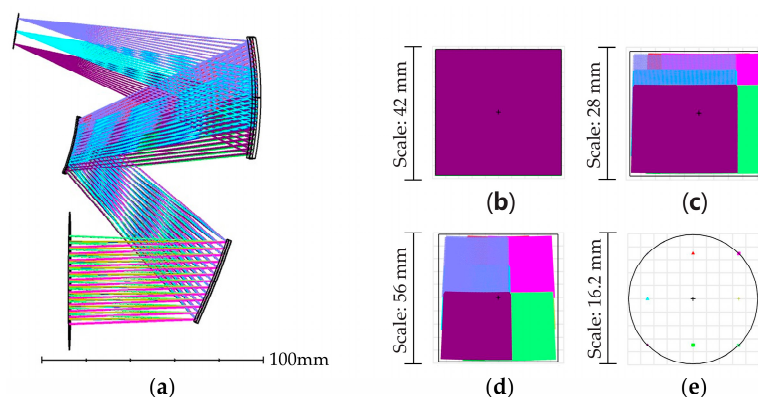
Figure 6. (**a**) The layout and the ray footprints of (**b**) the first, (**c**) the second, (**d**) the third mirror, and (**e**) the image of the final system with square aperture after optimization.

Table 4. The Chebyshev coefficients of M1~M3 of the final square aperture system.

Term	Chebyshev Polynomial	Coefficient of M1	Coefficient of M2	Coefficient of M3
1	$T_2 \cdot T_0$	3.09015×10^{-5}	3.80479×10^{-4}	7.77191×10^{-5}
2	$T_4 \cdot T_0$	7.75289×10^{-7}	6.54103×10^{-6}	-1.97742×10^{-7}
3	$T_6 \cdot T_0$	1.06861×10^{-9}	7.79002×10^{-9}	-9.66175×10^{-9}
4	$T_0 \cdot T_1$	-5.51300×10^{-5}	-8.41580×10^{-5}	-4.08245×10^{-5}
5	$T_2 \cdot T_1$	-2.48849×10^{-5}	-2.21547×10^{-5}	-1.39731×10^{-5}
6	$T_4 \cdot T_1$	2.27960×10^{-8}	1.72561×10^{-6}	-5.97034×10^{-8}
7	$T_0 \cdot T_2$	-3.63091×10^{-5}	-3.94105×10^{-4}	-8.35798×10^{-5}
8	$T_2 \cdot T_2$	2.10825×10^{-6}	-1.10960×10^{-6}	-4.71111×10^{-6}
9	$T_4 \cdot T_2$	4.07705×10^{-9}	-2.43633×10^{-7}	-8.94891×10^{-8}
10	$T_0 \cdot T_3$	-1.21726×10^{-5}	-1.73920×10^{-5}	-8.81040×10^{-6}
11	$T_2 \cdot T_3$	4.21215×10^{-8}	3.82503×10^{-6}	-2.45415×10^{-7}
12	$T_0 \cdot T_4$	3.51572×10^{-7}	-1.00236×10^{-6}	-2.14341×10^{-6}
13	$T_2 \cdot T_4$	6.67833×10^{-9}	-4.44205×10^{-7}	-1.22654×10^{-7}
14	$T_0 \cdot T_5$	6.91323×10^{-9}	1.02000×10^{-6}	-8.16191×10^{-8}
15	$T_0 \cdot T_6$	1.10858×10^{-9}	-2.51828×10^{-7}	-2.90451×10^{-8}

2.3. Design of Circular Diaphragm System

2.3.1. Specification of Circular Aperture Diaphragm System

Table 5 shows the design specifications for the off-axis three-mirror optical system equipped with a circular aperture diaphragm.

Table 5. Design specifications of optical system with circular aperture diaphragm.

Parameter	Specifications
Spectral band	0.4 μm~0.9 μm
FOV	$4° \times 4°$
Focal length	150 mm
Entrance pupil diameter	40 mm
F-number	3.75
Volume	$\leq 1 \ dm^3$
Detector pixel size	9.2 μm × 9.2 μm
Image spot size	$\leq$18.4 μm × 18.4 μm
Distortion	$\leq$1%

2.3.2. Optimization of Circular Aperture Diaphragm System

In order to compare with the square aperture diaphragm system, a circular aperture diaphragm system was designed. This system had the same FOV, volume, and spot size requirements as the square aperture system, with the only difference being the area of the entrance pupil. By comparing the two systems in Section 3, it is demonstrated that the square aperture diaphragm system, under the same detection performance (referring to the image spot size and energy concentration), can achieve a larger entrance pupil area while having a smaller volume.

Starting with the off-axis three-mirror system depicted in Figure 2 as the starting point, we set the system's aperture diaphragm to a circular aperture with a diameter of 40 mm while keeping all other parameters constant. In the optimization process, the image spot size served as the system metric for operand generation. After an initial optimization, contrast became the system metric for further operand generation. The sag departures of the data points were sampled at 12 polar angles across the maximum aperture, and the sag departures of adjacent data points were set to zero as manufacturing constraints [11]. Incorporating manufacturing constraints along with the default operands generated by the system, the optimization process was iterated multiple times until the system's performance meets the specified requirements. Ultimately, a sixth order even XY polynomial was derived. Figure 7 illustrates the optimization design workflow for the off-axis three-mirror system with a circular aperture diaphragm.
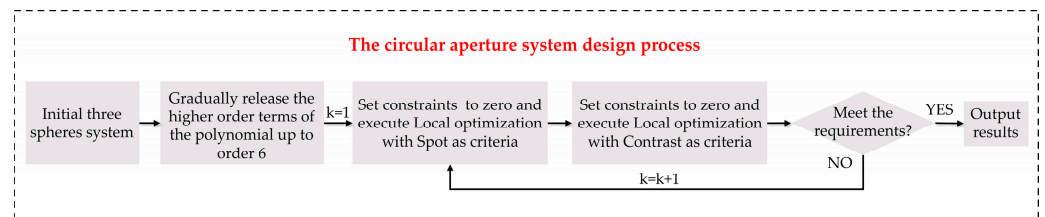
Figure 7. The design flow of the optimization process of adding constraints to the circular aperture diaphragm system.

In this scenario, the primary mirror featured a circular aperture diaphragm with a diameter of 40 mm. The radius of curvatures for the base spherical surfaces of mirrors M1, M2, and M3 were -333.962 mm, -143.829 mm, and -162.889 mm, respectively. The system had a focal length of 150mm and an FOV spanning $4°$ by $4°$. The volume of the circular aperture diaphragm system was $58 \times 148 \times 112$ mm^3, equating to 0.96 cubic decimeters, which is nearly equal to the preset requirement of 1 cubic decimeter. Figure 8 displays a three-dimensional view of the system along with the ray footprints on mirrors M1 to M3 and the image plane. Table 6 shows the coefficients of the XY polynomials for mirrors M1 to M3 of the final system with a circular aperture.
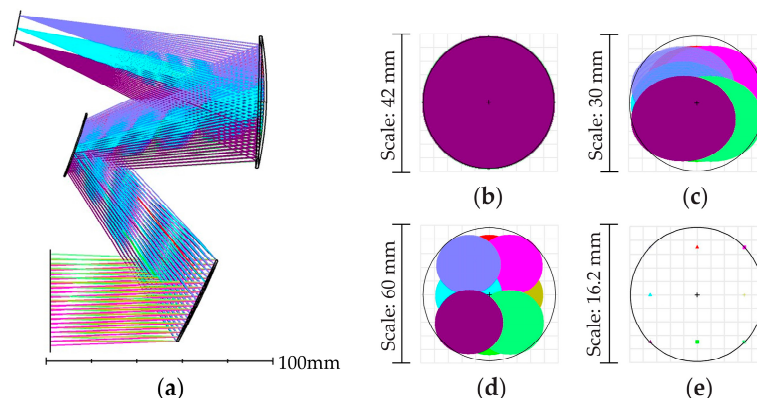
Figure 8. (**a**) The layout and the ray footprints of (**b**) the first, (**c**) the second, (**d**) the third mirror, and (**e**) the image of the final system with circular aperture after optimization.

Table 6. The XY polynomial coefficients of M1~M3 of the final circular aperture system.

Term	XY Polynomial	Coefficient of M1	Coefficient of M2	Coefficient of M3
1	X_0Y_1	-5.16382×10^{-3}	-2.65285×10^{-3}	2.07542×10^{-3}
2	X_2Y_0	7.51008×10^{-5}	-1.30409×10^{-4}	1.66844×10^{-4}
3	X_0Y_2	-2.43452×10^{-5}	-1.65974×10^{-3}	-2.27986×10^{-4}
4	X_2Y_1	-2.07191×10^{-6}	-4.75254×10^{-6}	-7.19401×10^{-7}
5	X_0Y_3	-2.02014×10^{-6}	-5.97744×10^{-6}	-1.07717×10^{-6}
6	X_4Y_0	7.38200×10^{-9}	2.38565×10^{-8}	2.64418×10^{-10}
7	X_2Y_2	8.45233×10^{-9}	-7.30961×10^{-8}	-1.36465×10^{-8}
8	X_0Y_4	2.07651×10^{-9}	-1.17743×10^{-7}	-1.40769×10^{-8}
9	X_4Y_1	5.29384×10^{-12}	3.11436×10^{-10}	-1.38869×10^{-11}
10	X_2Y_3	4.10040×10^{-12}	3.87430×10^{-10}	-5.69388×10^{-11}
11	X_0Y_5	3.67792×10^{-12}	3.74196×10^{-10}	-3.46940×10^{-11}
12	X_6Y_0	6.79070×10^{-14}	2.15218×10^{-14}	-1.03031×10^{-13}
13	X_4Y_2	1.23865×10^{-13}	-6.38676×10^{-12}	-9.15860×10^{-13}
14	X_2Y_4	1.46621×10^{-13}	-1.15496×10^{-11}	-1.25781×10^{-12}
15	X_0Y_6	5.04151×10^{-14}	-9.86376×10^{-12}	-6.49354×10^{-13}

3. Results

3.1. Comparison of Two Systems

This section offers an in-depth comparison of the design outcomes for both systems, examining their performance both pre- and post-defocusing.

Figure 9 presents the distribution of image spots across various fields of view for the two design configurations. For the square aperture diaphragm off-axis three-mirror system, the RMS diameter of the image spot across the full FOV was 0.56 μm, significantly smaller than the diffraction-limited Airy spot diameter of 5.4 μm and the detector image element size of 9.2 μm. It is crucial to clarify that the Airy spot diameter for a square aperture is calculated differently from that of a circular aperture. Here, the entrance pupil diameter is derived by considering the square pupil area as an equivalent circular area, using the circle's diameter as the equivalent pupil diameter, thus yielding an Airy spot diameter of 5.4 μm for the square aperture. The Airy spot diameter shown in Figure 9a of Zemax, calculated based on the square aperture's diagonal as the equivalent circular entrance pupil diameter, is 4.2 μm, which is not the actual Airy spot diameter for the square aperture system, but rather 5.4 μm. Figure 10a displays the energy concentration curves of the image spot on the optimal image plane of the system with a square aperture, with 80% of the energy concentrated within a diameter of 4.6 μm and 90% within a diameter of 9.2 μm.
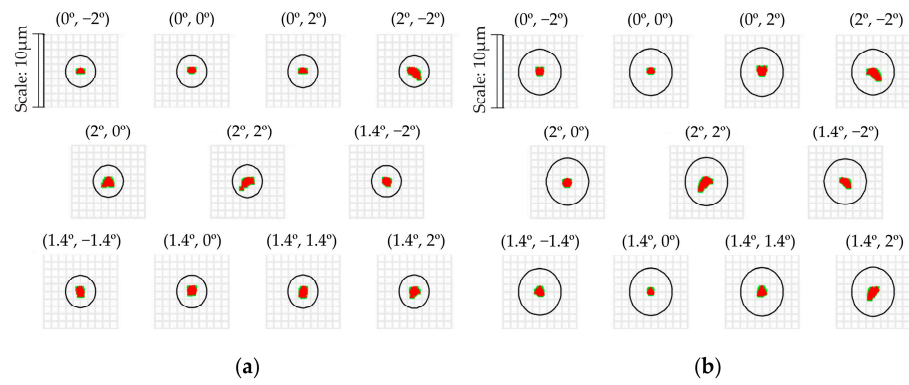
Figure 9. The spot diagrams of the system with (**a**) square aperture and (**b**) circular aperture before defocusing.
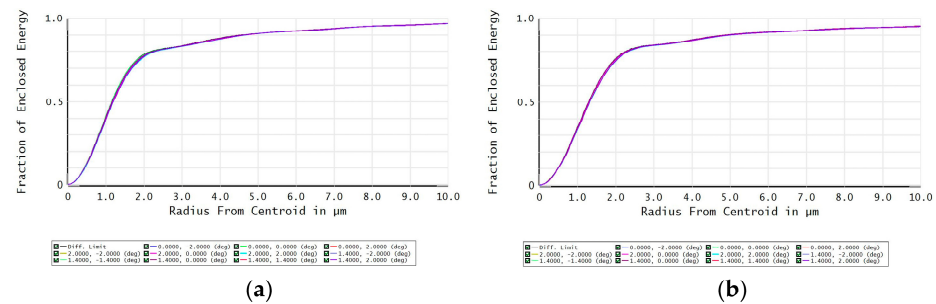
Figure 10. The energy concentration curves of the image spot on the optimal image plane of the system with (**a**) square aperture and (**b**) circular aperture before defocusing.

For the circular aperture diaphragm off-axis three-mirror system, the RMS diameter of the image spot across the full FOV was 0.52 μm, which is much smaller than the Airy spot diameter of 6 μm and the detector image element size of 9.2 μm. Figure 10b shows the energy concentration curves of the image spot on the optimal image plane of the system with circular aperture, where 80% of the energy is concentrated within a diameter of 4.6 μm, and 90% within a diameter of 9.2 μm.

Figure 11 shows the relative illuminance distributions of the square aperture diaphragm system and the circular aperture diaphragm system in different FOVs. The uniformity of illuminances in the image plane were 98% and 97%, respectively, which were obtained with excellent performance.
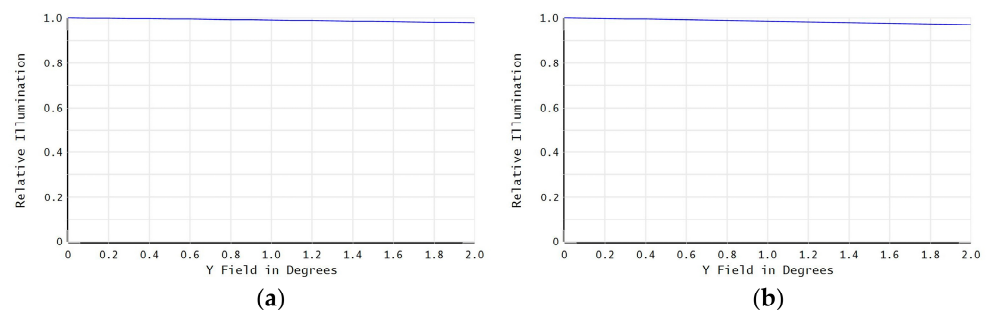
Figure 11. The relative illuminance distributions of the system with (**a**) square aperture and (**b**) circular aperture before defocusing.

Figure 12 shows the grid distortion of the square aperture diaphragm system and the circular aperture diaphragm system. The maximum distortions were 0.39% and 0.34%, respectively, which meet the design specifications.
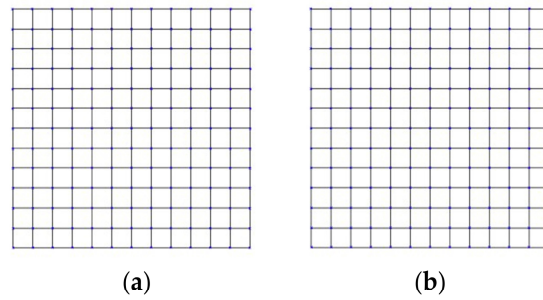
Figure 12. The grid distortions of the system with (**a**) square aperture and (**b**) circular aperture before defocusing.

Figure 13 shows the full field RMS wavefront error for the square aperture diaphragm system and the circular aperture diaphragm system. The maximum RMS wave errors were 0.039λ and 0.017λ, respectively.
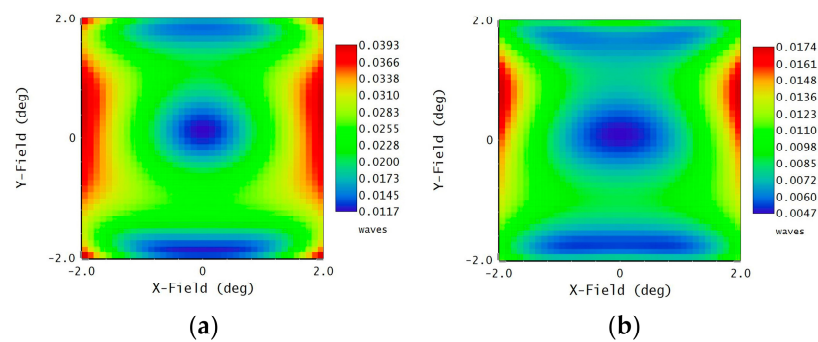
Figure 13. The full field wavefront errors of the system with (**a**) square aperture and (**b**) circular aperture before defocusing.

Since the image spot diameters at the optimal image plane positions were all smaller than the single image element size, in order to improve the position interpolation accuracy, the image spot diameter should be increased to 2 × 2 image elements by means of defocusing [28]. After both defocusing 0.07 mm, the geometric diameters of the image spot were both close to the 2 × 2 image element size, which meets the application requirements of the satellite-based detection optical system, as shown in Figure 14. At this time, Figure 15 shows the energy concentration curve of the image spot. For the square aperture diaphragm system, 80% of the energy is concentrated in the spot with a diameter of 16.6 μm, and 85% of the energy is concentrated in the spot with a diameter of 18.4 μm. For the circular aperture diaphragm, 80% of the energy is concentrated in the 15.6 μm diameter range and 85% of the energy is concentrated in the 18.4 μm diameter range. Both exhibit excellent performance.
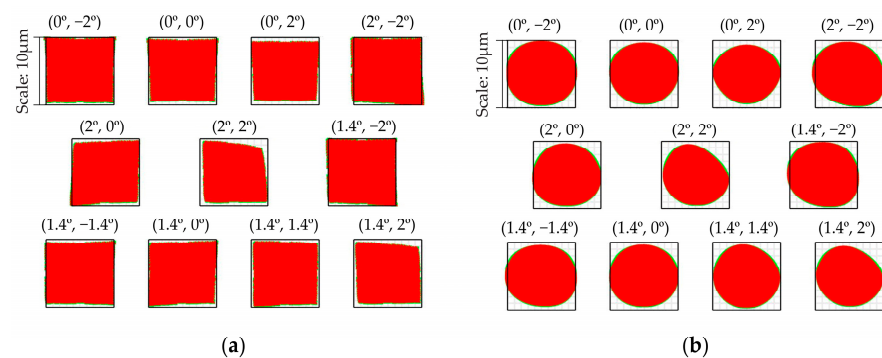
Figure 14. The spot diagrams of the system with (**a**) square aperture and (**b**) circular aperture after defocusing.
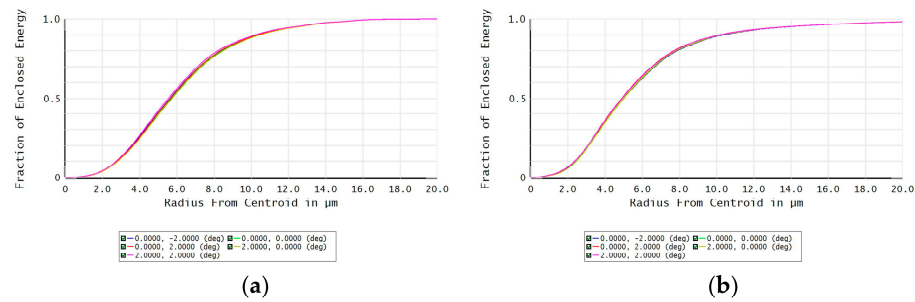
Figure 15. The energy concentration curves of the image spot on the optimal image plane of the system with (**a**) square aperture and (**b**) circular aperture after defocusing.

Figure 16 shows the distribution diagrams of sag departures between the freeform surface and base surface for M1~M3 of the square aperture diaphragm system and the circular aperture diaphragm system. The PV values of sag departures between mirrors M1~M3 and the base spheres were 0.06 mm, 0.28 mm, and 0.24 mm for the square system, and 0.24 mm, 0.43 mm, and 0.38 mm for the circular system, respectively. By adding manufacturing constraints, the PV values of the sag departures between mirrors M1~M3 and the base spheres reduced by 75%, 35%, and 37%, respectively, which greatly reduces the difficulty of surface measurement.
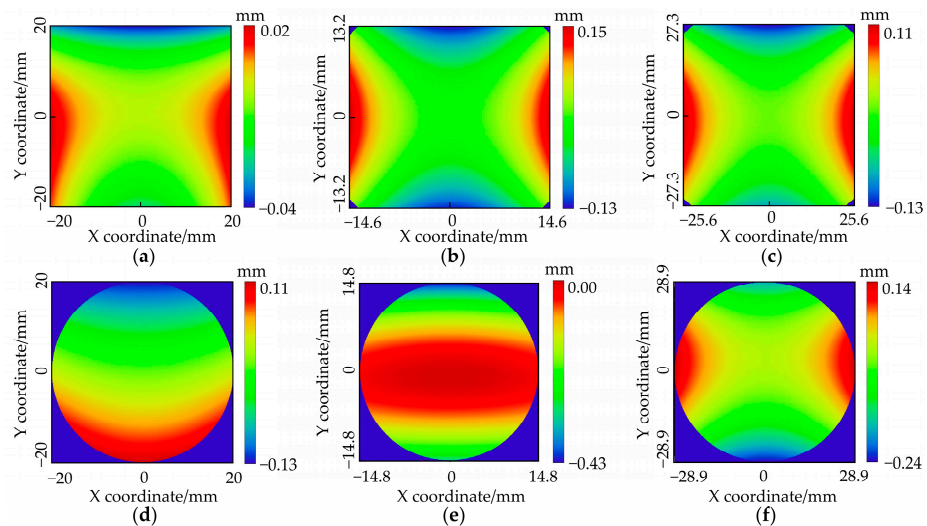
Figure 16. The distribution diagrams of sag departures of (**a**) the first, (**b**) the second, and (**c**) the third mirror between the freeform surface and base surface in the final square aperture system. The distribution diagrams of sag departures of (**d**) the first, (**e**) the second, and (**f**) the third mirror between the freeform surface and base surface in the final circular aperture system.

Summarizing the comparative results of the two systems, it was found that the square aperture diaphragm system had a larger entrance pupil area (1600 mm^2 versus 1257 mm^2) while having a smaller system volume (0.78 cubic decimeters versus 0.96 cubic decimeters) and at least a 35% decrease in sag departures. Other system specifications, such as the FOV and focal length, were the same for both systems, and the spot size and energy concentration were nearly identical. Consequently, as per Equation (1), the system exhibited a higher equivalent magnitude by 0.24, which enabled it to detect fainter space targets.

3.2. Tolerance Analysis of the Two Systems After Defocusing

The energy concentrations of the systems after defocusing within an image plane diameter of 18.4 μm, which is equivalent to twice the pixel size, serve as the metric for our merit function in the tolerance analysis. At standard manufacturing and assembly levels,

the tolerance distribution for each mirror, as detailed in Table 7, is adhered to for both square and circular aperture diaphragm systems.

Table 7. Distributions of tolerances.

Parameter	M1 (Diaphragm)	M2	M3
Curvature radius (mm)	±0.05	±0.05	±0.05
RMS Machining accuracy (λ = 632.8 nm)	±1/30	±1/30	±1/30
Top spacing deviation (mm)	±0.2	±0.2	±0.2
Decenter X (mm)	±0.025	±0.025	±0.025
Decenter Y (mm)	±0.025	±0.025	±0.025
Tilt X (arc minute)	±2	±2	±2
Tilt Y (arc minute)	±2	±2	±2
Tilt Z (arc minute)	±3	±3	±3
Compensation method	Image plane position (M3 back focal length)and image plane tilt		

Under the aforementioned tolerance constraints, Figure 17 illustrates the feasibility of energy concentration at different wavelengths and fields of view following 500 Monte Carlo simulations. For the defocused square aperture diaphragm system, there was a 90% probability that the energy concentration value within 18.4 μm (twice the pixel size) on the image plane exceeded 87.0%. For the defocused circular aperture diaphragm system, there was a 90% probability that the energy concentration value within 18.4 μm (twice the pixel size) on the image plane exceeded 85.2%. The tolerance analysis results confirmed that both systems were capable of fulfilling the requirements for visible light target detection.
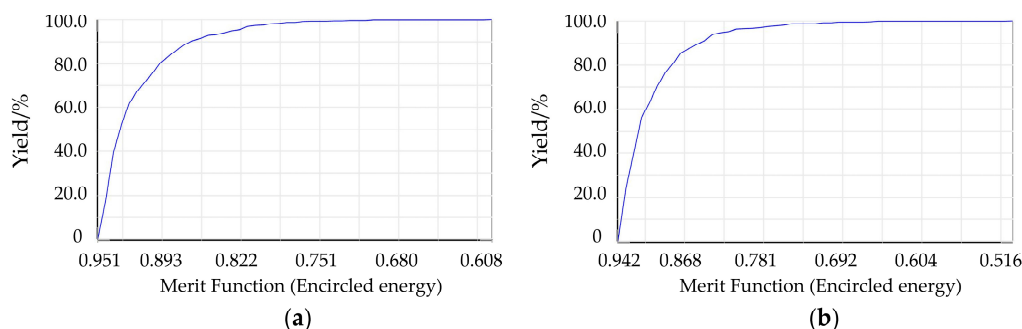
Figure 17. A total of 500 Monte Carlo simulations of the system (**a**) with square aperture and (**b**) circular aperture after defocusing (the horizontal axis represents the diffraction energy concentration, while the vertical axis represents the probability corresponding to a specific diffraction energy concentration).

4. Discussion

It is widely accepted that increasing a system's aperture size results in larger ray footprints on subsequent optical surfaces. Consequently, with larger mirror diameters, the system's volume tends to increase, especially when constrained by considerations such as potential mirror collisions. The circular aperture diaphragm system presented in this study exemplifies this principle, with its volume nearly reaching the upper limit of the specified requirements. It stands to reason that opting for a larger entrance pupil diameter would likely result in a system volume that surpasses the preset requirements. Meanwhile, the square aperture diaphragm system, which is circumscribed around the circle, can deliver a larger entrance pupil area while maintaining a smaller volume, as well as having comparable manufacturing and assembly complexity. This better meets the needs of satellite-based systems for high detection sensitivity.

We attribute the benefits of the square aperture diaphragm system to the more efficient utilization of the mirror surfaces by this system. Figures 6b and 8b illustrate the ray footprints in the X direction, which range from $-2°$ to $2°$, and in the Y direction, which span from $-2°$ to $2°$. The full field-of-view ray footprints are constructed by mapping the ray footprints from all fields, excluding the (0, 0) field, onto the YOZ plane centered on the mirror. It is evident that the circular aperture diaphragm system leaves a larger portion of the mirror unused, while the square aperture diaphragm system maximizes the utilization of the mirror surface area. Consequently, the square aperture diaphragm system not only expands the entrance pupil area to boost detection sensitivity for space targets, but also accomplishes this feat within a more compact system volume.

This paper presents a design case for a square aperture diaphragm freeform surface optical system for space target detection in the visible light spectrum, highlighting the ability of the square aperture diaphragm to enhance the detection sensitivity of satellite-based systems. Notably, this enhancement in area is achieved without compromising the system's compactness, as the volume remains relatively smaller. This finding contributes to the evolution of space target detection by providing a promising avenue for further development in the field.

Although the square aperture diaphragm system designed in this paper has undergone tolerance analysis, with 500 Monte Carlo simulations indicating that under standard manufacturing and assembly practices, there is a 90% probability that the system's energy concentration within 18.4 μm (twice the pixel size) on the image plane will be greater than 87.0%, making it feasible for fabrication and assembly. However, we recognize that there is often a gap between the actual fabricated and assembled system and the design specifications. Therefore, our next step is to design a CGH detection optical path for rectangular mirrors, proceed with the actual fabrication of three rectangular mirrors, and conduct assembly. During this process, we will identify any issues and redesign the system as necessary until the fabricated and assembled system meets the required performance criteria. In addition, within the framework of our upcoming research endeavors, we will carry out comprehensive and in-depth investigations into the realms of material selection as well as structural design. The overarching objective of these efforts is to optimize the overall weight of the system, thereby enhancing its performance and practical applicability in a more holistic sense.

5. Conclusions

This paper introduces a design of a high-sensitivity square aperture diaphragm freeform optical system, meticulously engineered for the detection of space targets in the visible light spectrum. The system stands out with a 40 mm $\times$ 40 mm square entrance pupil, a $4° \times 4°$ FOV, and a 150 mm focal length. The spot size is limited to a 2×2 pixel area, with 85% of the energy concentrated within 18.4 μm. Compared to a circular aperture diaphragm system with equivalent specifications, the square aperture diaphragm system, with a 27% larger entrance pupil area (1600 mm^2 versus 1257 mm^2) while having a smaller system volume (0.78 cubic decimeters versus 0.96 cubic decimeters), yields a 0.24 magnitude improvement for space targets. This advancement significantly enhances the system's detection sensitivity, enabling it to detect even fainter space targets. Our work, as presented in this paper, not only meets the stringent requirements for satellite-based systems but also sets a new course for the evolution of future satellite-based detection technologies.

References

1. Sun, H.; Wei, M.; Luo, C. Design Research of the Space Debris Monitoring Database Management System. *Digit. Commun. World* **2016**, *3*, 70–74.
2. Zhu, G. Space activity in Russia in 2012. *Space Int.* **2013**, *2*, 32–41.
3. Yang, C. Optical Antenna Design and Stray Light Research based on Inter-Satellites Laser Communication Terminal. Master's Thesis, Changchun Institute of Optics, Fine Mechanics and Physics, Chinese Academy of Sciences, Changchun, China, 2017.
4. Harrison, D.C.; Chow, J.C. Space-Based Visible sensor on MSX satellite. *Eng. Phys.* **1994**, *2217*, 377–387.
5. Goldstein, N.; Dressler, R.A.; Shroll, R.; Richtsmeier, S.; Mclean, J.; Dao, P.; Murray-Krezan, J.; Fulcoly, D. Ground testing of prototype hardware and processing algorithms for a Wide Area Space Surveillance System (WASSS). *J. Opt.* **2015**, *17*, 5.
6. Bauer, A.; Schiesser, E.M.; Rolland, J.P. Starting geometry creation and design method for freeform optics. *Nat. Commun.* **2018**, *9*, 1756. [CrossRef] [PubMed]
7. Hicks, R.A. Controlling a ray bundle with a free-form reflector. *Opt. Lett.* **2008**, *33*, 1672–1674. [CrossRef]
8. Miñano, J.C.; Benítez, P.; Lin, W.; Infante, J.; Muñoz, F.; Santamaría, A. An application of the SMS method for imaging designs. *Opt. Express* **2009**, *17*, 24036–24044. [CrossRef] [PubMed]
9. Yang, T.; Zhu, J.; Hou, W.; Jin, G. Design method of freeform off-axis reflective imaging systems with a direct construction process. *Opt. Express* **2014**, *22*, 9193–9205. [CrossRef] [PubMed]
10. Gao, R.; Mao, X.; Li, J.; Xu, Z.; Xie, Y. Freeform off-axis four-mirror all-aluminum infrared detection system (invited). *Infrared Laser Eng.* **2023**, *52*, 20230338.
11. Cai, Z.; Li, J.; Yu, J.; Huang, C.; Xie, Y.; Mao, X. Optical freeform reflective imaging system design method with manufacturing constraints. *Appl. Opt.* **2023**, *62*, 6480–6490. [CrossRef] [PubMed]
12. Ning, M.; Mao, X.; Yu, J.; Yuan, Y.; Yang, J.; Cai, Z.; Xie, Y. Design of compact off-axis three-mirror freeform optical system with small F number. In *AOPC 2023: Optical Design and Manufacturing*; SPIE: San Diego, CA, USA, 2023; Volume 129640.
13. Xie, Y.; Mao, X.; Li, J.; Wang, F.; Wang, P.; Gao, R.; Li, X.; Ren, S.; Xu, Z.; Dong, R. Optical design and fabrication of an all-aluminum unobscured two-mirror freeform imaging telescope. *Appl. Opt.* **2020**, *59*, 833–840. [CrossRef]
14. Li, X.; Ni, D.; Yang, M.; Ren, Z. Design of Large Field of View Space Camera Optical System Based on Freeform Surfaces. *Acta Photonica Sin.* **2018**, *47*, 0922003.
15. Ren, C.; Meng, Q. Design Method for Freeform Off-Axis Three-Mirror Anastigmat Optical Systems with a Large Field of View and Low Error Sensitivity. *Photonics* **2024**, *11*, 211. [CrossRef]
16. Wang, B.; Wang, X.; Jiang, H.; Wang, Y.; Yang, C.; Meng, Y. Design of a Spaceborne, Compact, Off-Axis, Multi-Mirror Optical System Based on Freeform Surfaces. *Photonics* **2024**, *11*, 51. [CrossRef]
17. Fan, C.; Kong, L.; Yang, B.; Wan, X. Design of Dual-Focal-Plane AR-HUD Optical System Based on a Single Picture Generation Unit and Two Freeform Mirrors. *Photonics* **2023**, *10*, 1192. [CrossRef]
18. Jia, B.; Li, Y.; Lv, Q.; Jin, F.; Tian, C. Design of a Large Field of View and Low-Distortion Off-Axis Optical System Based on a Free-Form Surface. *Photonics* **2023**, *10*, 506. [CrossRef]
19. Mao, X.; Li, H.; Han, Y.; Luo, Y. Two-step design method for highly compact three-dimensional freeform optical system for LED surface light source. *Opt. Express* **2014**, *22*, A1491–A1506. [CrossRef] [PubMed]
20. Cheng, Y. Study on Design and Application of Freeform Optics. Doctoral Dissertation, Tianjin University, Tianjin, China, 2013.

21. Wu, C.; Yan, C.; Liu, W.; Zhang, J. Prism Hyperspectral Imaging Optical System Design with Rectangular Aperture. *Acta Opt. Sin.* **2013**, *33*, 228–234.

22. Zhou, L.; Yang, T.; Cheng, D.; Wang, Y. Design method of imaging systems using square-domain orthogonal polynomials freeform surface (invited). *Infrared Laser Eng.* **2023**, *52*, 20230317.

23. Lan, C. Modeling and Detecting Capability Analysis of Space-Based Space Object Optical Observation System. Doctoral Dissertation, Information Engineering University, Zhengzhou, China, 2009.

24. Li, F.; Zheng, L.; Yan, F.; Xue, D.; Zhang, X. Optical testing method and its experiment on freeform surface with computer-generated hologram. *Infrared Laser Eng.* **2012**, *44*, 1052–1056.

25. Yang, T.; Zhu, J.; Wu, X.; Jin, G. Direct design of freeform surfaces and freeform imaging systems with a point-by-point three-dimensional construction-iteration method. *Opt. Express* **2015**, *23*, 10233–10246. [CrossRef]

26. Zhu, J.; Wu, X.; Yang, T.; Jin, G. Generating optical freeform surfaces considering both coordinates and normals of discrete data points. *J. Opt. Soc. Am. A* **2014**, *31*, 2401–2408. [CrossRef]

27. Yang, T.; Zhu, J.; Jin, G. Design of freeform imaging systems with linear field-of-view using a construction and iteration process. *Opt. Express* **2014**, *22*, 3362–3374. [CrossRef] [PubMed]

28. Zhao, Y. New Type Reflective Optical System Design for A Star Sensor. Master's Thesis, Harbin Institute of Technology, Harbin, China, 2007.